Coupled Reforming of Methane to Syngas ($2H_2$-CO) over Mg-Al Oxide Supported Ni Catalyst

Maoshuai Li, André C. van Veen*

School of Engineering, The University of Warwick, Coventry, CV4 7AL, United Kingdom

*Corresponding author:
Tel: +44(0)2450933; email: Andre.vanVeen@warwick.ac.uk

Graphical Abstract

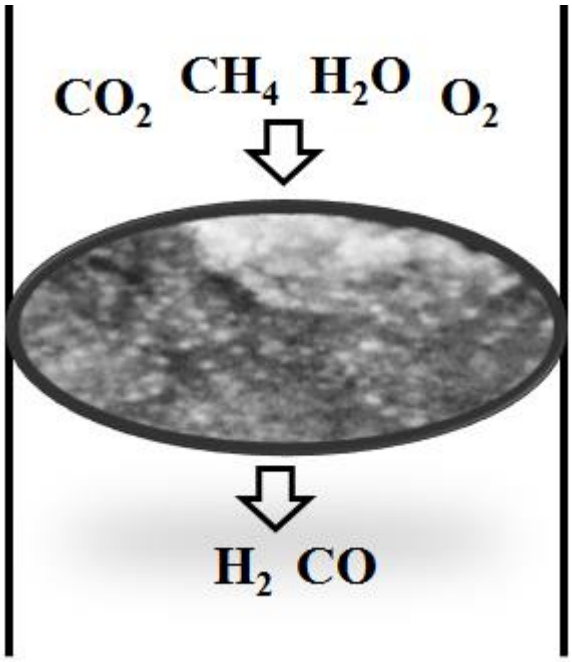

Highlights

1. Bi-reforming and coupled reforming of methane to syngas established over Ni catalyst.
2. CH_4 and CO_2 conversions, close to thermodynamic equilibrium, were achieved.
3. Coupled reforming delivered higher CH_4 conversion and enhanced stability than bi-reforming.
4. Temporal activity loss in bi-reforming can be linked to carbon deposition.

Abstract

We report bi-reforming and coupled reforming of methane with carbon dioxide, steam and/or oxygen to produce syngas over Ni supported on Mg-Al mixed oxide. The catalyst has been characterised in terms of specific surface area, TPR, XRD, TGA-DTG, SEM and TPO-MS analysis. Ni/Mg-Al mixed oxide exhibited Ni particle size range (11-30 nm) with a mean of 20.7 nm. Syngas H_2/CO = 2.0, suitable for methanol/Fischer-Tropsch fuel synthesis, has been achieved for both reactions (T = 1048 K, P = 1 atm). The impact of process parameters including temperature, feeding concentration and GHSV on conversion and H_2/CO ratio has been demonstrated. The Ni catalyst suffered temporal activity decline in bi-reforming that can be linked to formation of carbon whiskers encapsulated Ni particles resulting in a loss of active sites. Coupled reforming delivered higher CH_4 conversion and enhanced stability, but lower CO_2 conversion than bi-reforming under similar conditions. The enhanced stability in coupled reforming can be attributed to lower carbon deposition on Ni particles due to combustion of carbon by oxygen.

***Key words*:** syngas; methane; carbon dioxide; coupled reforming; supported Ni; carbon deposition

1. Introduction

Conversion of methane and carbon dioxide, two major greenhouse gases, to valuable chemicals has great significance in terms of global energy security and climate change [1, 2]. Reforming of these gases to syngas, a critical intermediate in the manufacture of hydrogen, ammonia, methanol and Fischer-Tropsch products represents a promising route [3]. A variety of reforming reactions including

$$CH_4 + CO_2 \longrightarrow 2H_2 + 2CO \quad \textbf{(1)}$$

$$3CH_4 + CO_2 + O_2 \longrightarrow 6H_2 + 4CO \quad \textbf{(2)}$$

$$3CH_4 + CO_2 + 2H_2O \longrightarrow 8H_2 + 4CO \quad \textbf{(3)}$$

dry reforming (Eq.1), oxy-CO_2 reforming (Eq.2) and bi-reforming (Eq.3) have been studied in the existing literature [4-6]. Bi-reforming to produce syngas offer significant advantages over dry reforming and oxy-CO_2 reforming with respect to (I) flexibility in H_2/CO ratio adjustment for downstream chemical (e.g., methanol, Fischer-Tropsch fuel) synthesis and (II) decreased carbon deposition due to presence of steam [1]. Olah et al. have demonstrated achievement of syngas (H_2/CO = 2.0), suitable for methanol synthesis, and stable activity with 320 h on-stream for high pressure (7-42 atm) bi-reforming reaction over Ni/MgO (1103 K, 6.0×10^4 cm^3 h^{-1} g_{cat}^{-1}) [7, 8]. Reaction at atmospheric pressure delivered syngas H_2/CO = 2.1 over Ni-based pyrochlore catalyst (1023 K, 9.8×10^4 cm^3 h^{-1} g_{cat}^{-1}) [9] and H_2/CO = 2.0 over (Al_2O_3 [10], MgO-Al_2O_3 [11] and CeO_2 [12]) supported Ni (1023-1073 K, 5.3×10^5 cm^3 h^{-1} g_{cat}^{-1}). In addition to Ni based catalyst, bimetallic Ru-Ni (supported on MgO) [13] and Ru/$ZnLaAlO_4$ [14] have been examined in bi-reforming reaction to enhance catalyst resistance to carbon deposition.

$$4CH_4 + CO_2 + H_2O + O_2 \longrightarrow 9H_2 + 5CO \quad \textbf{(4)}$$

Coupled reforming (Eq.4), combined exothermic methane oxidation with bi-reforming, represents an alternative route for syngas production. Relative to bi-reforming, coupled reforming is more energy efficient due to heat release from methane oxidation [1, 15]. Use of oxygen provides higher level of oxidant that can address carbon deposition, a critical cause of catalyst deactivation in methane reforming reaction [16]. Coupled reforming of methane to syngas, target at $H_2/CO = 2$ has not been studied to any significant extent. A search through literature found reported studies on coupled reforming of methane over Ni/MgO [17] and tri-reforming over (MgO [18], SiO_2 [19] and CeO_2-ZrO_2 [20]) supported Ni catalysts, producing syngas $H_2/CO = 1.5$-3.0 (973-1123 K).

For methane reforming reactions, catalysts based on noble metals exhibit high catalytic stability and great resistance to coke formation [21]. However, high cost restricts industrial scale application. Inexpensive Ni based catalysts have been used in reforming reaction due to high activity comparable to noble metals, but suffered rapid deactivation because of Ni particle agglomeration and carbon deposition [22]. MgO as basic support can enhance CO_2 chemisorption [23]. Inclusion of Al_2O_3 can increase surface area. Moreover, Ni supported on Mg-Al mixed oxide have been shown to bear strong metal-support interaction to suppress Ni sintering and exhibits enhanced catalytic stability in methane reforming reaction [24-26]. In this study, we for the first time examine coupled reforming of methane with steam, carbon dioxide and oxygen to produce syngas $H_2/CO = 2$ at atmospheric pressure over Mg-Al mixed oxide supported Ni catalyst and provide a comparison of catalytic performance to bi-reforming. We also evaluate carbon deposition in both reactions as one critical consideration for catalyst stability.

2. Experimental

2.1 Materials and catalyst preparation

Mg-Al mixed oxide was prepared by co-precipitation of metal nitrates (Sigma Aldrich, >98%) with aqueous ammonia (10% w/w, Fisher) and ammonium carbonate (VWR Chemicals, 31.4% Assay NH_3) using flow synthesis. Aqueous nitrate salts (Mg^{2+} = 1.5 M, Mg/Al = 3/1, 100 cm^3) and a mixture (100 cm^3) of ammonia (5 M) with ammonium carbonate (0.25 M) was delivered separately via teflon line using a peristaltic pump (ISMATEC) at a fixed flow rate (1.5 cm^3 min^{-1}), mixed in a tee (bore = 1.8 mm) and transported continuously to 50 cm^3 water. The suspension was stirred (500 rpm) at 353 K for 2 h. The solid obtained was separated by filtration, washed with distilled water and dried at 393 K overnight. The dried sample was calcined in air at 873 K (10 K min^{-1}) for 4 h. Nickel (15% w/w) on Mg-Al mixed oxide was prepared by deposition-precipitation using aqueous ammonia. An aqueous solution of nickel nitrate (0.25 M, 100 cm^3) and ammonia (0.6 M, 100 cm^3) was added to the support (8 g). The suspension was stirred and heated to 353 K. The solid obtained was separated by filtration, washed with distilled water and dried at 393 K overnight. The catalyst precursor was sieved (ATM fine test sieves) to 60-200 mesh and activated at 10 K min^{-1} to 1073 K in 10 cm^3 min^{-1} H_2 (BOC, 99.99%) for characterisation.

2.2 Catalyst characterisation

Nitrogen physisorption was performed on the Micromeritics ASAP 2020 system and total specific surface area (SSA) was calculated using the standard BET method with pore volume obtained from BJH desorption. Prior to analysis, samples were vacuumed and outgassed at 573 K for 1 h. Nickel content was measured by inductive coupled plasma optical emission spectroscopy (ICP-OES, PerkinElmer

5300DV) from the diluted extract in HNO_3. Temperature programmed reduction (TPR) was conducted in a quartz tube cell. The sample was heated in 84 cm^3 min^{-1} 5% v/v H_2/Ar at 6 K min^{-1} to 1073 K and held for 1 h. Hydrogen consumption was monitored by a thermal conductivity detector (TCD). X-ray diffractograms (XRD) were recorded on a Bruker D5005 X-ray diffractometer using Cu Kα radiation. Samples were scanned at 0.02º $step^{-1}$ over the range $30º \leq 2\theta \leq 80º$ at ambient temperature and the diffractograms identified against the JCPDS-ICDD reference standards, *i.e.* Ni (04-0850), MgO (89-7746), γ-Al_2O_3 (10-0425) and $MgAl_2O_4$ (77-1193). Nickel particle morphology (size and shape) and carbon deposition was examined by Zeiss Supra 55VP field emission scanning electron microscopy (SEM). Mean metal size (*d*) was based on a count of up to 500 particles. Thermogravimetric-derivative thermogravimetric analysis (TGA-DTG) of the samples post-reaction was performed on a simultaneous thermal analyser (NETZSCH STA449) by monitoring temporal mass with temperature. The samples (*ca.* 30 mg) were heated in 50 cm^3 min^{-1} air to 1073 K (at 10 K min^{-1}). TPO-MS analysis of the spent catalysts was conducted in a quartz tube by recording CO_2 signal with time and temperature on a Pfeiffer OMNIStar mass spectrometer. The samples (*ca.* 15 mg) were heated in 20 cm^3 min^{-1} 10% O_2/Ar to 1073 K (at 5 K min^{-1}).

2.3 Catalytic procedures

Catalyst testing was conducted at atmospheric pressure (973-1073 K), *in situ* after activation, in a continuous flow fixed bed (alumina) tubular reactor (i.d. = 8 mm). The schematic diagram of the reactor and gas analysis system is shown in **Fig.1**. The catalyst (5-30 mg) was mixed with ground quartz (60-200 mesh) and sandwiched between quartz wool. A layer of quartz particles was placed on the top of quartz wool

before the catalyst bed. Reaction temperature was monitored by a thermocouple inserted in the catalyst bed. Water was delivered to the reactor using a Shimadzu HPLC (LC-20AD) pump and vaporized to steam in the upper part of the reactor. Reactant gases (CH_4, CO_2 and/or O_2, BOC, 99.99%), N_2 (BOC, 99.99%) as internal standard and Ar (BOC, 99.99%) as balance gas were introduced to reactor by Brooks mass flow controller (SLA5800 series) at (reactant) gas hourly space velocity (GHSV) = 2×10^4 - 2×10^5 h^{-1}. For all reactions, the flow rate of methane was fixed at 9 cm^3 min^{-1}. The reactor effluent was condensed in a gas sample cooler (Bühler) for subsequent analysis using online gas chromatography (Shimadzu 2014) equipped with a 0.5 cm^3 sampling loop, thermal conductive detector (TCD) and flame ionization detector (FID), employing serial Hayesep Q (3.0 m × 2.1 mm i.d.) and Molecular Sieve 5A packed columns (2.0 m × 2.1 mm i.d.). Data acquisition and manipulation were performed using GCsolution Lite (Version 2.4) chromatography data system. Reactant i (i = CH_4 or CO_2) conversion (X_i) is calculated by the change of volumetric flow rate

$$X_i\ (\%) = \frac{Q_{[reactant]i,\ in} - Q_{[reactant]i,\ out}}{Q_{[reactant]i,\ in}} \times 100 \qquad \textbf{(5)}$$

where subscripts "in" and "out" refer to inlet and outlet gas streams. In blank tests, passage of reactant gases to empty reactor did not result in any detectable conversion. Repeated reactions delivered data reproducibility and carbon balance within 7%.

3. Results and discussion

3.1 Catalyst characterisation

Sample physicochemical properties are presented in **Table 1**. The specific surface area (SSA) and pore volume of activated Ni/Mg-Al mixed oxide (127 m^2 g^{-1}, 0.29 cm^3 g^{-1}) is lower than the support (172 m^2 g^{-1}, 0.51 cm^3 g^{-1}) and can be attributed

to a partial pore filling during catalyst preparation [27]. The values are in good agreement with those reported for Ni supported on Mg-Al mixed oxide in the literature [26, 28]. TPR profile of Ni/Mg-Al mixed oxide (**Fig. 2(I)**) exhibited a reduction peak at the extended time, where hydrogen consumption (**Table 1**) is in good agreement with that (1.0 mol mol_{Ni}^{-1}) required for the $Ni^{2+} \rightarrow Ni^{0}$ step. Düdder et al. reported a single TPR peak (T_{max} = 943-1188 K) during activation (6 K min^{-1}) of $Ni/MgAlO_x$ with a shift to higher temperature with lowering Ni content (50 → 1 mol%) [29]. Oemar et al. [30] have ascribed TPR signal in the temperature range (673-773 K) to reduction of NiO species bearing weak interaction with oxide support and high temperature (>873 K) peak to NiO species that have strong metal-support interaction in the TPR analysis (10 K min^{-1}) of Ni/SBA-15. XRD analysis (**Fig. 2(II)**) revealed three diffraction signals at 2θ = 44.5°, 51.9° and 76.6° corresponding to Ni (111), (200) and (220) planes. Additional peaks at 2θ = 36.9°, 43.0°, 62.5° and 78.8° can be attributed to cubic MgO [31]. There was no clearly discernible peak for magnesium aluminate spinel (2θ = 31.3°, 36.9°, 44.8°, 59.4 and 65.2°) and γ-Al_2O_3 (2θ = 39.5°, 45.9° and 67.0°), which may be due to masking by stronger signals of MgO and Ni and/or below detection limit. Nickel particle size is critical in determining carbon formation/accumulation and catalyst stability in methane reforming [32]. Representative SEM image and associated Ni particle size distribution histogram (**Fig. 3**) revealed that the sample exhibited pseudo-spherical Ni particles with a size range (11-30 nm) and mean (20.7 nm, **Table 1**). This value is smaller than that (54.2 nm) reported by Hadian et al. for (15% w/w) Ni impregnated on $MgAl_2O_4$ [24].

3.2 Catalysis of bi-reforming

Thermodynamic analysis of bi-reforming demonstrates that $CH_4/(H_2O+CO_2)$ = 0.9-1.2 and high temperature (≥ 973 K) facilitates conversion of CH_4 and CO_2 [33]. The reaction was initially carried out at 1048 K using a feeding ratio of $CH_4/H_2O/CO_2$ = 3/2.2/1.2. Representative time on-stream conversion and H_2/CO ratio profiles for bi-reforming are shown in **Fig. 4**. An initial decrease in activity was observed with steady conversion (CH_4 = 73%, CO_2 = 64%) attained after 8 h on-stream. Although activities cannot be directly compared due to different conditions, our conversions are higher than that (CH_4 = 52-60%, CO_2 = 48-52%) reported elsewhere [9], but lower than the corresponding equilibrium conversions (CH_4 = 94%, CO_2 = 77%) [33]. Methane and carbon dioxide were solely converted to syngas with no detectable by-products (e.g., alkane and/or alkene), indicative of 100% selectivity to CO (based on CH_4). H_2/CO ratio fluctuated within the 1.99-2.03 range with a mean value of 2.01 achieved under the reaction condition employed. This meets the requirement for methanol/Fischer-Tropsch fuel synthesis and circumvents extra adjustment of H_2/CO ratio when compared to methane dry reforming (H_2/CO = 1) and steam reforming (H_2/CO = 3).

To understand bi-reforming, the impact of process parameters including temperature, CH_4/H_2O feeding ratio and GHSV on catalytic activity and H_2/CO ratio were examined and presented in **Fig. 5**. An increase in temperature from 973 K to 1073 K (**AI**) resulted in higher conversion of CH_4 (52% → 78%) and CO_2 (39% → 68%), consistent with the nature of endothermic reaction. The conversions were lower than the equilibrium values. H_2/CO ratio decreased (2.22 → 1.95) with increasing temperature (**AII**). Higher temperature favors methane dry reforming that generates lower amounts of H_2 relative to steam reforming. This can account for decreased H_2/CO ratio observed at higher temperature. Water serves as hydrogen donors in

steam reforming, which can impact on hydrogen production [34]. We considered evaluation of varying water concentration (presented as molar CH_4/H_2O ratio) on activity and H_2/CO adjustment (**Fig. 5(B)**). A three-fold increase in CH_4 conversion with a consequently decreased CO_2 conversion (to 50%) was observed with increasing water feeding (CH_4/H_2O: 3/0 → 3/3, **BI**). This suggests a competition of dry reforming with steam reforming, where steam reforming predominates in the presence of excess water. Increasing water concentration served to enhance H_2/CO ratio (1.00 → 2.25, **BII**), confirming the role of water in adjusting H_2/CO. We can note that H_2/CO = 1 obtained at CH_4/H_2O = 3/0 equals to the reaction stoichiometry of methane dry reforming (Eq.1). This demonstrates an increase in water feeding switched the reaction from exclusive dry reforming to predominant steam reforming. To this point, bi-reforming of methane to produce syngas H_2/CO = 2 has been established. However, conversion was still low. The possibility of decreasing GHSV by increasing catalyst amount was considered as a means of enhancing conversions of methane and carbon dioxide. The profiles shown in **Fig. 5(C)** revealed that both conversions increased (up to 87% for CH_4 and 81% for CO_2) with lowering GHSV (13.6×10^4 → 2.8×10^4 h^{-1}). The values at GHSV = 2.8×10^4 h^{-1} were close to the equilibrium conversions (CH_4 = 94%, CO_2 = 77%) [33]. H_2/CO did not vary significantly, maintaining within 1.99-2.01. This suggests variation in GHSV did not change the equilibrium between steam and dry reforming, and lower GHSV promoted both reactions.

3.3 Catalysis of coupled reforming

To probe autothermal reaction condition for the coupled reforming, net heat change (ΔHr) was analysed as a function of temperature and CH_4/O_2; the result is shown in **Fig. 6**. Regardless of CH_4/O_2, the net heat of the reaction increased with

increasing temperature (973 → 1073 K), indicating an increase in the reaction endothermicity and/or a decrease in the exothermicity. This can be attributed to higher temperature favors endothermic (dry and steam) reforming of methane. With an increase in oxygen feeding (CH_4/O_2: 4/0 → 4/2), the value of net heat went from positive to negative, suggesting a move from endothermal to exothermal zone. This can be linked to increased oxygen feeding promoting exothermic methane oxidation. Net heat balance ($\Delta Hr = 0$) was observed at CH_4/O_2 = 4/1 and 1023 K.

Representative time on-stream conversion and H_2/CO ratio profiles for the coupled reforming are shown in **Fig. 7**. In contrast to bi-reforming, stable conversions, e.g., CH_4 = 81%, CO_2 = 52% and O_2 = 100%, were maintained within 24 h on-stream, indicative of no apparent catalyst deactivation. There is consensus that presence of oxygen serves to limit carbon deposition with enhanced catalytic stability for reforming reactions [35]. Coupled reforming of methane has not been examined in detail with few studies available for direct comparison. But we can note 96% and 40% conversion for CH_4 and CO_2, reported by Choudhary et al. for reaction at higher temperature (1123 K) and lower GHSV (4.8×10^4 h^{-1}) [17]. Compared to bi-reforming, coupled reforming delivered higher CH_4 conversion, but lower CO_2 conversion under similar conditions. This can be to some extent attributed to complete combustion of methane to carbon dioxide. Syngas was the sole product. H_2/CO ratio (mean = 1.99), close to 2.0 was maintained for 24 h on-stream with no obvious fluctuation. This value was lower than that (mean = 2.01) obtained in bi-reforming. Our results have established coupled reforming of methane to syngas with H_2/CO = 2.

In common to bi-reforming, higher conversion of CH_4 (up to 94%) and CO_2 (up to 74%) were observed at elevated temperature (**Fig. 8(AI)**). The conversions at 1073 K were close to the equilibrium values. Oxygen was completely converted at

any temperature, consistent with the equilibrium conversions. It should be noted that CO_2 conversion was down to 3% at 973 K, suggesting low temperature does not facilitate CO_2 activation and conversion. H_2/CO ratio decreased dramatically (2.27 → 1.98) from 973 K to 1073 K (**Fig. 8(AII)**), consistent with that observed in bi-reforming reaction (**Fig. 5(A)**). In common to water effect on bi-reforming (**Fig. 5(B)**), an increase in water feeding (CH_4/H_2O: 4/0 → 4/3) served to enhance CH_4 conversion (70% → 93%) with steady conversion attained at higher feeding (CH_4/H_2O: 4/3-4/4). This suggests use of excess water (three times higher than the reaction stoichiometry) does not further promote methane steam reforming. A consequential decrease (95% → -12%) in CO_2 conversion was observed with increasing water feeding (**Fig. 8(BI)**). Negative CO_2 conversion at CH_4/H_2O = 4/4, also reported in Choudhary's study [17], can be attributed to that dry reforming was suppressed with lower CO_2 conversion and/or methane steam reforming with CO_2 generation was promoted, resulting in net formation of CO_2. Full conversion of oxygen was obtained at any CH_4/H_2O. In common to bi-reforming, lower water feeding generated less amount of hydrogen, resulting in decreased H_2/CO ratio (**Fig. 8(BII)**). For reaction conducted in absence of steam (CH_4/H_2O = 4/0), H_2/CO equaled to the reaction stoichiometry (1.5) of Oxy-CO_2 reforming (Eq. 2). Oxygen can participate in CH_4 oxidation, CO oxidation and/or carbon combustion in the coupled reforming [4], which impact on activity and H_2/CO ratio. The influence of oxygen feeding content (presented as molar CH_4/O_2 ratio) was examined and presented in **Fig. 8(C)**. A decrease in oxygen feeding (CH_4/O_2: 4/2 → 4/0) lowered CH_4 conversion (95% → 59%) and enhanced CO_2 conversion (-17% → 81%). Negative CO_2 conversion observed at CH_4/O_2 = 4/2 can be attributed to excess oxygen promoted methane combustion resulting in net formation of CO_2. H_2/CO ratio was decreased (2.07 → 1.90) with decreasing O_2 feeding, consistent with Choudhary's

observation [17]. Choudhary et al. [17] concluded that H_2/CO ratio was determined by steam reforming, partial oxidation and dry reforming, occurring to different extents depending upon the process conditions. We can attribute decreased H_2/CO to dry reforming predominated over steam reforming with less H_2 generation. A decrease in GHSV from 8.7×10^4 h^{-1} to 4.4×10^4 h^{-1} resulted in enhanced conversions of CH_4 and CO_2 (up to 96% for CH_4 and 63% for CO_2, **Fig. 8(DI)**). CH_4 and CO_2 conversions tended to be constant with a further decrease in GHSV (to 2.9×10^4 h^{-1}) due to thermodynamic equilibrium control. In contrast to bi-reforming, H_2/CO decreased (1.99 → 1.86) with decreasing GHSV (**Fig. 8(DII)**). Olah et al. [8] have observed decreased H_2/CO (<2) at lower GHSV in high pressure bi-reforming reaction, but without specifying a reason. We can tentatively attribute the decreased H_2/CO to predominance of methane combustion and dry reforming in the reaction network.

3.4 Catalyst characterisation post-reaction

Catalyst deactivation due to carbon deposition and Ni sintering was a feature of methane reforming reaction [16, 36]. Catalysts post bi-reforming (**Fig. 4**) and coupled reforming (**Fig. 7**) were subjected to characterisation measurements to study catalyst deactivation. A slight increase in SSA and decrease in pore volume was recorded over the spent catalysts (**Table 1**), which can be a consequence of carbon accumulation. TGA result (**Fig. 9**) revealed that the spent catalyst after the coupled reforming exhibited a lower (by 3%) mass loss relative to bi-reforming in the whole investigated temperature range (298-1073 K). A calculation demonstrated the amount of carbon deposition equaled to 0.23-0.24% of total carbon feeding. Derivative plots for the spent samples demonstrated four steps occurred during weight loss. Both spent samples exhibited a similar (2-2.3% w/w) mass loss at $T \leq 393$ K due to water removal. Mass loss at higher temperature (*ca*. 473 K) can be attributed to desorption of

adsorbed reactants (e.g., H_2O, CO_2 and CH_4) and removal of easily oxidisable carbonaceous species as reported elsewhere [37]. Amorphous carbon and/or graphic type carbon contribute to the mass loss at 660 K [38]. Additional weight loss at 783 K for the sample post bi-reforming and at 873 K for the spent catalyst post coupled reforming can be attributed to combustion of different types of whisker carbon [39]. Carbon deposition on the catalyst surface was further confirmed by SEM analysis (**Fig. 10A**). Significant amount of carbon whiskers were detected on the catalyst surface post bi-reforming (**IA**). A number of Ni particles were encapsulated on the end of carbon whiskers. In methane reforming, methane dissociation ($CH_4 \rightarrow C + 2H_2$) and Boudouard reaction ($2CO \rightarrow CO_2 + C$) are main carbon formation reactions, where the former is more significant at temperature >873 K [40, 41]. Djinović et al. [42] studying carbon formation in dry reforming of methane over Ni/Al_2O_3, reported that encapsulating carbon leading to loss of Ni active surface was responsible for catalyst deactivation. Moreover, Ni particle size distribution histogram for the catalyst post bi-reforming (**Fig. 10 (IB)**) revealed a wider Ni size range (11-90 nm) and larger mean (33.9 nm) relative to the fresh catalyst (11-30 nm, mean = 20.7 nm), suggesting severe Ni particle agglomeration and sintering during reaction. The spent catalyst for coupled reforming (**IIB**) exhibited the same Ni size range (11-90 nm), but a smaller mean (26.5 nm) than that for the catalyst post bi-reforming, suggesting slower sintering. TPO-MS measurement (**Fig. 11**) used to analyse carbon deposition revealed one low-temperature exothermic peak due to the removal of amorphous carbon and/or graphic carbon at 659 K for the spent catalysts post both reactions. Additional high-temperature exothermic signal due to combustion of carbon whisker was observed at 746 K for the catalyst post bi-reforming and at 844 K for the catalyst post coupled reforming. TPO-MS analysis again confirmed formation of amorphous/graphic

carbon and carbon whisker. In this study, carbon generated from methane dissociation on Ni surface, subsequent growth to whiskers and encapsulation of Ni particles, and severe Ni sintering can be linked to the initial decrease of activity in bi-reforming reaction. Less carbon formation and slower Ni sintering contributes to enhanced stability in the coupled reforming.

4. Conclusion

We have established bi-reforming and coupled reforming of methane with carbon dioxide, steam and/or oxygen to produce syngas (H_2/CO = 2.0) over Ni particles (mean = 20.7 nm) supported on Mg-Al mixed oxide. Higher conversions were observed at elevated temperature and lower GHSV for both reactions. Increased water feeding served to generate greater hydrogen with enhanced H_2/CO. Coupled reforming delivered higher CH_4 conversion and enhanced stability than bi-reforming under similar conditions, but with lower CO_2 conversion. The temporal activity loss in bi-reforming can be linked to carbon deposition (on the basis of TGA-DTG, TPO-MS and SEM analysis).

Acknowledgement

This work was financially supported by European Commission 7th Framework program: BIOGO project (Grant No. 604296). We are grateful to Dr. Nicolay Cherkasov, Prof. Shanwen Tao and Steve J. York for the contribution to TPO-MS, TGA-DTG and SEM analysis, respectively.

References

[1] N. Kumar, M. Shojaee, J.J. Spivey, Curr. Opin. Chem. Eng. 9 (2015) 8-15.

[2] J.M. Lavoie, Front. Chem. 2 (2014).

[3] N. Abatzoglou, C. Fauteux-Lefebvre, Wiley Interdiscip. Rev. Energy Environ. 5 (2016) 169-187.

[4] T.V. Choudhary, V.R. Choudhary, Angew. Chem. Int. Ed. 47 (2008) 1828-1847.

[5] M. Usman, W. Daud, H.F. Abbas, Renew. Sust. Energ. Rev. 45 (2015) 710-744.

[6] G.A. Olah, A. Goeppert, M. Czaun, G.K.S. Prakash, J. Am. Chem. Soc. 135 (2013) 648-650.

[7] G.A. Olah, G.K.S. Prakash, A. Goeppert, M. Czaun, T. Mathew, J. Am. Chem. Soc. 135 (2013) 10030-10031.

[8] G.A. Olah, A. Goeppert, M. Czaun, T. Mathew, R.B. May, G.K.S. Prakash, J. Am. Chem. Soc. 137 (2015) 8720-8729.

[9] N. Kumar, A. Roy, Z. Wang, E.M. L'Abbate, D. Haynes, D. Shekhawat, J.J. Spivey, Appl. Catal. A: Gen 517 (2016) 211-216.

[10] K.Y. Koo, H.S. Roh, U.H. Jung, W.L. Yoon, Catal. Today 185 (2012) 126-130.

[11] K.Y. Koo, H.S. Roh, U.H. Jung, D.J. Seo, Y.S. Seo, W.L. Yoon, Catal. Today 146 (2009) 166-171.

[12] H.S. Roh, K.Y. Koo, W.L. Yoon, Catal. Today 146 (2009) 71-75.

[13] M.A. Alvarez, M.A. Centeno, J.A. Odriozola, Top. Catal. 59 (2016) 303-313.

[14] Y. Khani, Z. Shariatinia, F. Bahadoran, Chem. Eng. J. 299 (2016) 353-366.

[15] V.R. Choudhary, K.C. Mondal, T.V. Choudhary, Appl. Catal. A: Gen 306 (2006) 45-50.

[16] O. Muraza, A. Galadima, Int. J. Energ. Re. 39 (2015) 1196-1216.

[17] V.R. Choudhary, B.S. Uphade, A.S. Mamman, Appl. Catal. A: Gen 168 (1998) 33-46.

[18] C.S. Song, P. Wei, Catal. Today 98 (2004) 463-484.

[19] A.J. Majewski, J. Wood, Int. J. Hydrogen Energy 39 (2014) 12578-12585.

[20] R.K. Singha, S. Das, M. Pandey, S. Kumar, R. Bal, A. Bordoloi, Catal. Sci. Technol. 6 (2016) 7122-7136.

[21] D. Pakhare, J. Spivey, Chem. Soc. Rev. 43 (2014) 7813-7837.

[22] S. Kawi, Y. Kathiraser, J. Ni, U. Oemar, Z.W. Li, E.T. Saw, ChemSusChem 8 (2015) 3556-3575.

[23] A. Serrano-Lotina, L. Daza, Appl. Catal. A: Gen 474 (2014) 107-113.

[24] N. Hadian, M. Rezaei, Z. Mosayebi, F. Meshkani, J. Nat. Gas Chem. 21 (2012) 200-206.

[25] C.J. Liu, J.Y. Ye, J.J. Jiang, Y.X. Pan, ChemCatChem 3 (2011) 529-541.

[26] Y.J. Zhu, S.H. Zhang, B.B. Chen, Z.S. Zhang, C. Shi, Catal. Today 264 (2016) 163-170.

[27] S. Jujjuri, E. Ding, S.G. Shore, M.A. Keane, J. Mol. Catal. A: Chem. 272 (2007) 96-107.

[28] M. Li, X. Wang, S.R. Li, S.P. Wang, X.B. Ma, Int. J. Hydrogen Energy 35 (2010) 6699-6708.

[29] H. Düdder, K. Kähler, B. Krause, K. Mette, S. Kühl, M. Behrens, V. Scherer, M. Muhler, Catal. Sci. Technol. 4 (2014) 3317-3328.

[30] U. Oemar, Y. Kathiraser, L. Mo, X.K. Ho, S. Kawi, Catal. Sci. Technol. 6 (2016) 1173-1186.

[31] M. Li, Y. Hao, F. Cárdenas-Lizana, M.A. Keane, Catal. Commun. 69 (2015) 119-122.

[32] K.O. Christensen, D. Chen, R. Lodeng, A. Holmen, Appl. Catal. A: Gen 314 (2006) 9-22.

[33] W.J. Jang, D.W. Jeong, J.O. Shim, H.M. Kim, H.S. Roh, I.H. Son, S.J. Lee, Appl. Energ. 173 (2016) 80-91.

[34] T.L. LeValley, A.R. Richard, M.H. Fan, Int. J. Hydrogen Energy 39 (2014) 16983-17000.

[35] H. Harju, J. Lehtonen, L. Lefferts, Catal. Today 244 (2015) 47-57.

[36] H.J. Wu, V. LaParola, G. Pantaleo, F. Puleo, A.M. Venezia, L.F. Liotta, Catalysts 3 (2013) 563-583.

[37] J.J. Guo, H. Lou, H. Zhao, D.F. Chai, X.M. Zheng, Appl. Catal. A: Gen 273 (2004) 75-82.

[38] A. Kambolis, H. Matralis, A. Trovarelli, C. Papadopoulou, Appl. Catal. A: Gen 377 (2010) 16-26.

[39] H. Arbag, S. Yasyerli, N. Yasyerli, G. Dogu, T. Dogu, Appl. Catal. B: Environ 198 (2016) 254-265.

[40] M.A. Ermakova, D.Y. Ermakov, A.L. Chuvilin, G.G. Kuvshinov, J. Catal. 201 (2001) 183-197.

[41] A.F. Cunha, J.J.M. Orfao, J.L. Figueiredo, Int. J. Hydrogen Energy 34 (2009) 4763-4772.

[42] P. Djinović, I.G.O. Ĉrnivec, B. Erjavec, A. Pintar, Appl. Catal. B: Environ 125 (2012) 259-270.

Table 1: Ni loading, specific surface area (SSA), total pore volume, TPR H_2 consumption and Ni particle size (from SEM analysis) of the fresh and spent catalysts.

	Ni loading (% w/w)	SSA ($m^2\ g^{-1}$)	Pore volume ($cm^3\ g^{-1}$)	H_2 consumption ($mol\ mol_{Ni}^{-1}$)	Size range (nm)	*d* (nm)
Fresh	15.4	127	0.29	0.93	11-30	20.7
Spent I[a]	-	136	0.27	-	11-90	33.9
Spent II[b]	-	130	0.25	-	11-90	26.5

a: spent catalyst post bi-reforming; b: spent catalyst post coupled reforming

Figure caption

Fig. 1: Schematic diagram of experimental setup

Fig. 2: (I) TPR profile and (II) XRD pattern for Ni/Mg-Al mixed oxide (Δ MgO, ♦ Ni, □ $MgAl_2O_4$ spinel).

Fig. 3: Representative SEM imagine and Ni size distribution histogram for Ni/Mg-Al mixed oxide.

Fig. 4: Conversions of methane (■), carbon dioxide (●) and H_2/CO ratio (♦) with time on-stream in the bi-reforming of methane (T = 1048 K, $CH_4/H_2O/CO_2$ = 3/2.2/1.2, GHSV = 8.6×10^4 h^{-1}, dash line: equilibrium value).

Fig. 5: Variation of (I) conversions (square: CH_4, circle: CO_2) and (II) H_2/CO ratio with (A) temperature ($CH_4/H_2O/CO_2$ = 3/2.2/1.2, GHSV = 8.6×10^4 h^{-1}); (B) CH_4/H_2O feeding ratio (T = 1048 K, CH_4/CO_2 = 3/1.2) and (C) GHSV (T = 1048 K, $CH_4/H_2O/CO_2$ = 3/2.2/1.2) in the bi-reforming of methane (solid: experimental value, open: equilibrium value).

Fig. 6: Analysis of net heat change (ΔHr) as a function of temperature and CH_4/O_2 (4/2 (▲), 4/1 (■) and 4/0 (●); $CH_4/H_2O/CO_2$ = 4/1.6/1).

Fig. 7: Conversions of methane (■), carbon dioxide (●), oxygen (▲) and H_2/CO ratio (♦) with time on-stream in the coupled reforming of methane (T = 1048 K, $CH_4/H_2O/CO_2/O_2$ = 4/1.6/1/1, GHSV = 8.7×10^4 h^{-1}, dash line: equilibrium value).

Fig. 8: Variation of (I) conversions (square: CH_4, circle: CO_2, triangle: O_2) and (II) H_2/CO ratio with (A) temperature ($CH_4/H_2O/CO_2/O_2$ = 4/1.6/1/1, GHSV = 8.7×10^4 h^{-1}); (B) CH_4/H_2O feeding ratio (T = 1048 K, $CH_4/CO_2/O_2$ = 4/1/1); (C) CH_4/O_2 feeding

ratio (T = 1048 K, $CH_4/H_2O/CO_2$ = 4/1.6/1) and (D) GHSV (T = 1048 K, $CH_4/H_2O/CO_2/O_2$ = 4/1.6/1/1) in the coupled reforming of methane (solid: experimental value, open: equilibrium value).

Fig. 9: TGA and DTG analysis for catalysts post bi-reforming (solid line) and coupled reforming (dash line).

Fig. 10: (A) Representative SEM imagines and (B) Ni size distribution histogram for catalysts post (I) bi-reforming and (II) coupled reforming.

Fig. 11: TPO-MS profile for catalysts post bi-reforming (solid line) and coupled reforming (dash line).

Fig. 1

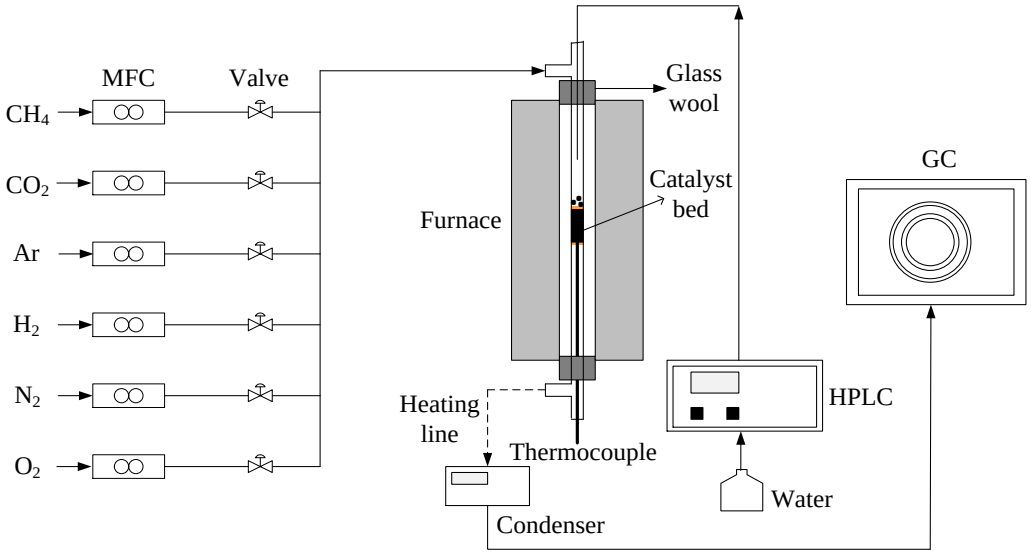

Fig. 2

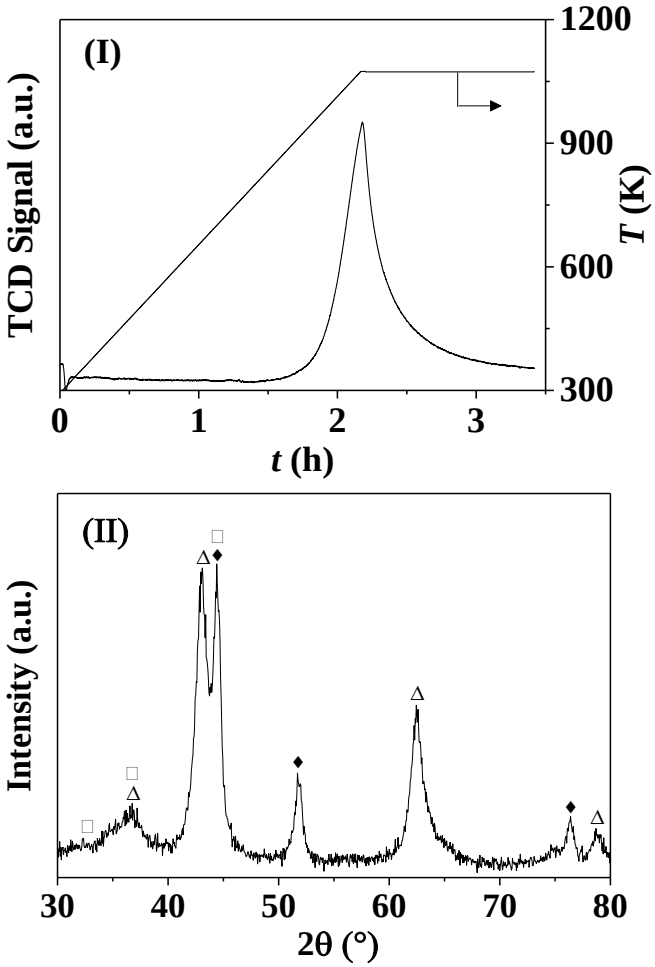

Fig. 3

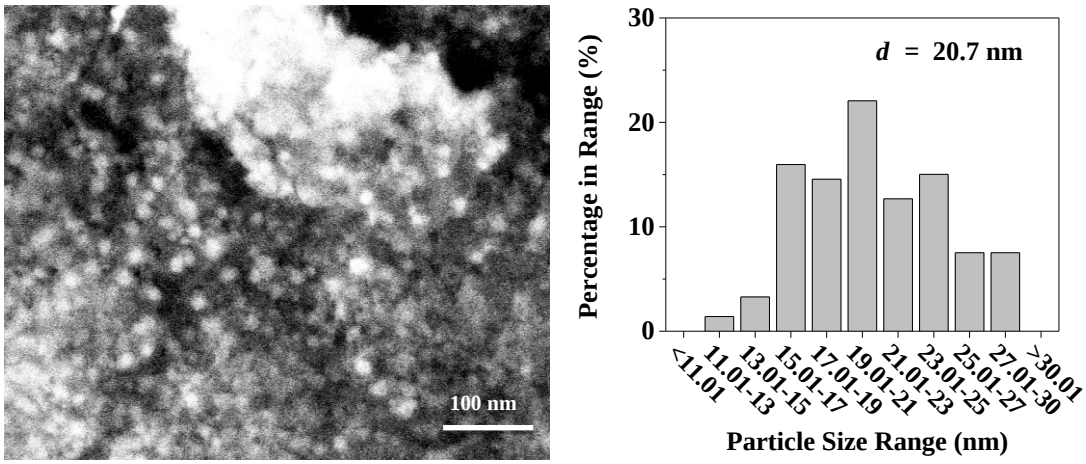

Fig. 4

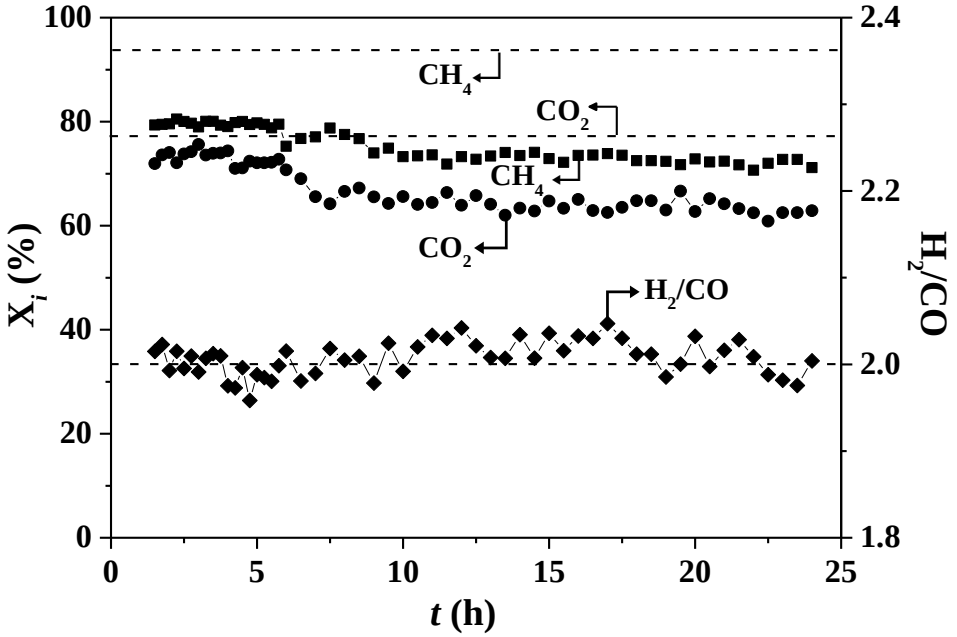

Fig. 5

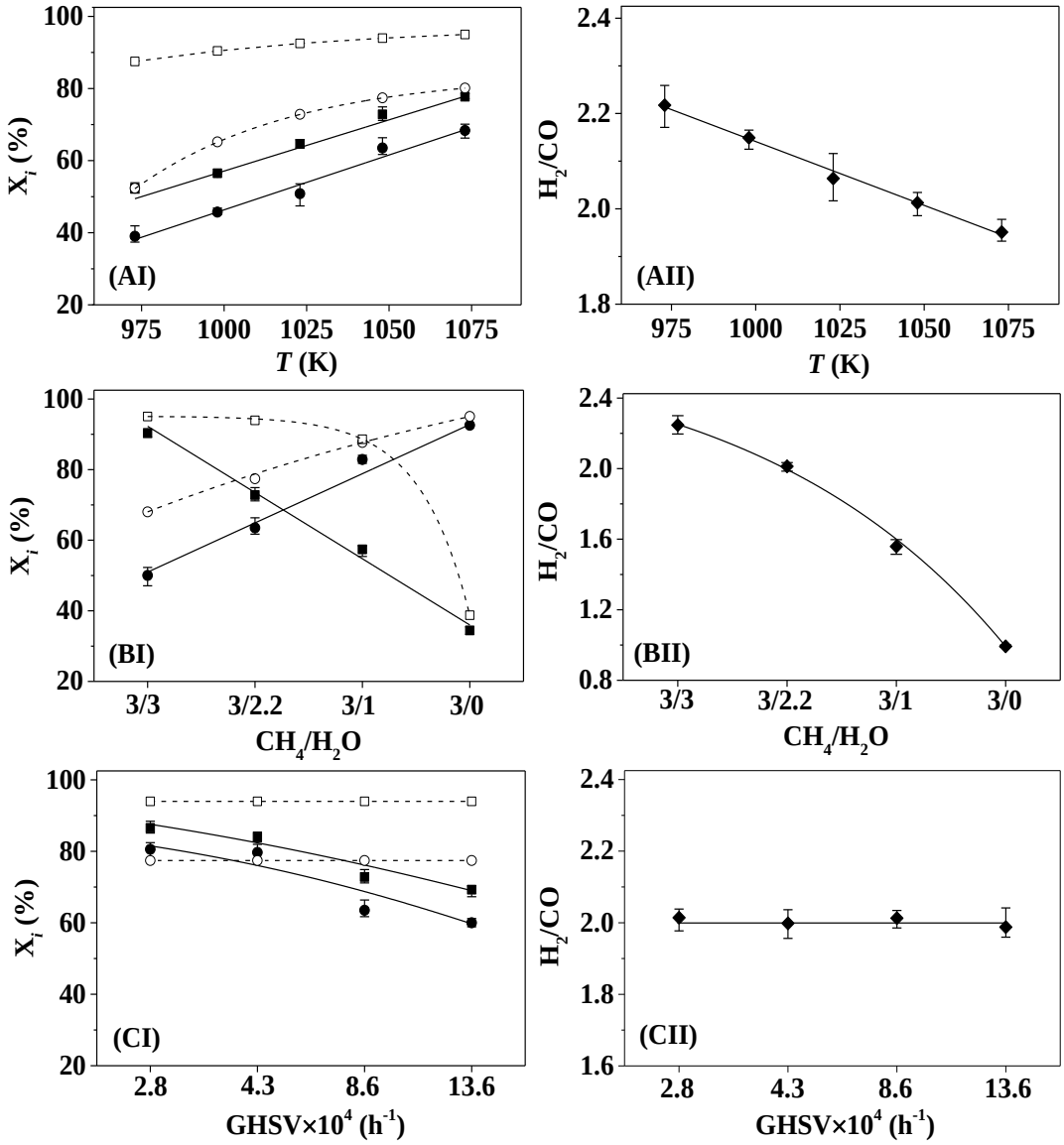

Fig. 6

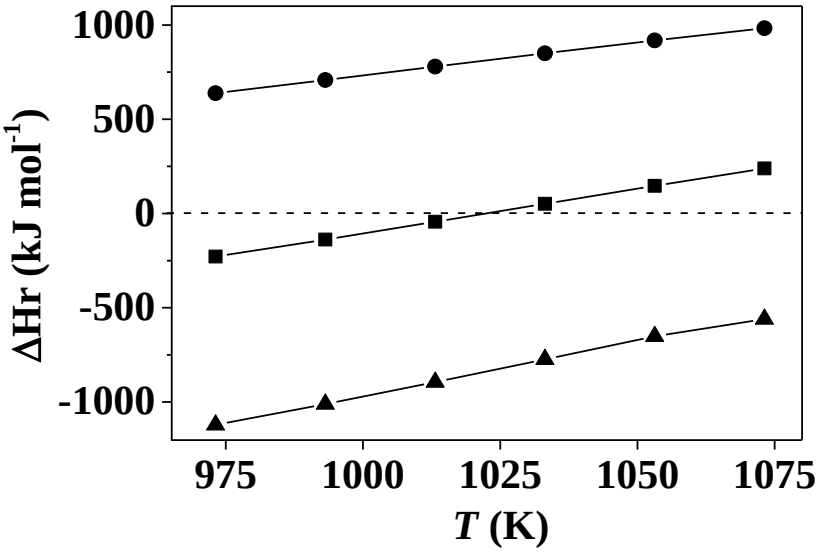

Fig. 7

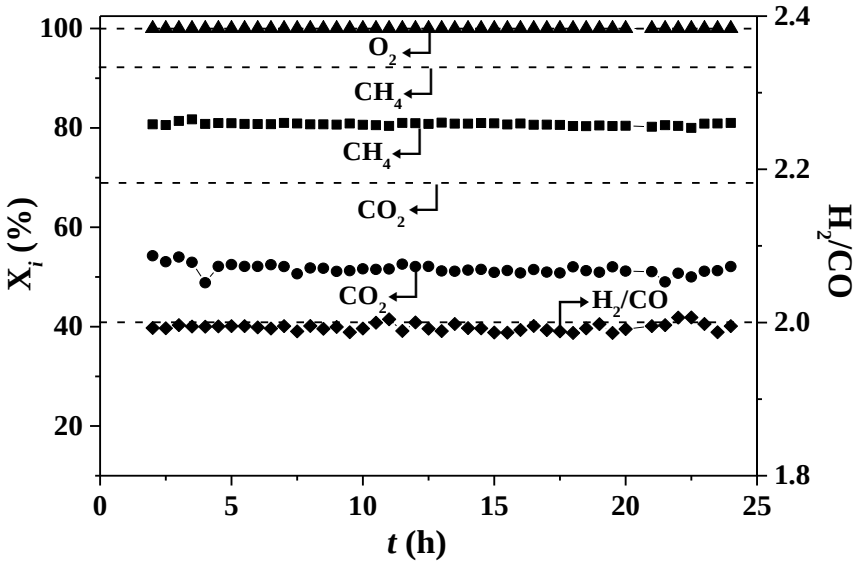

Fig. 8

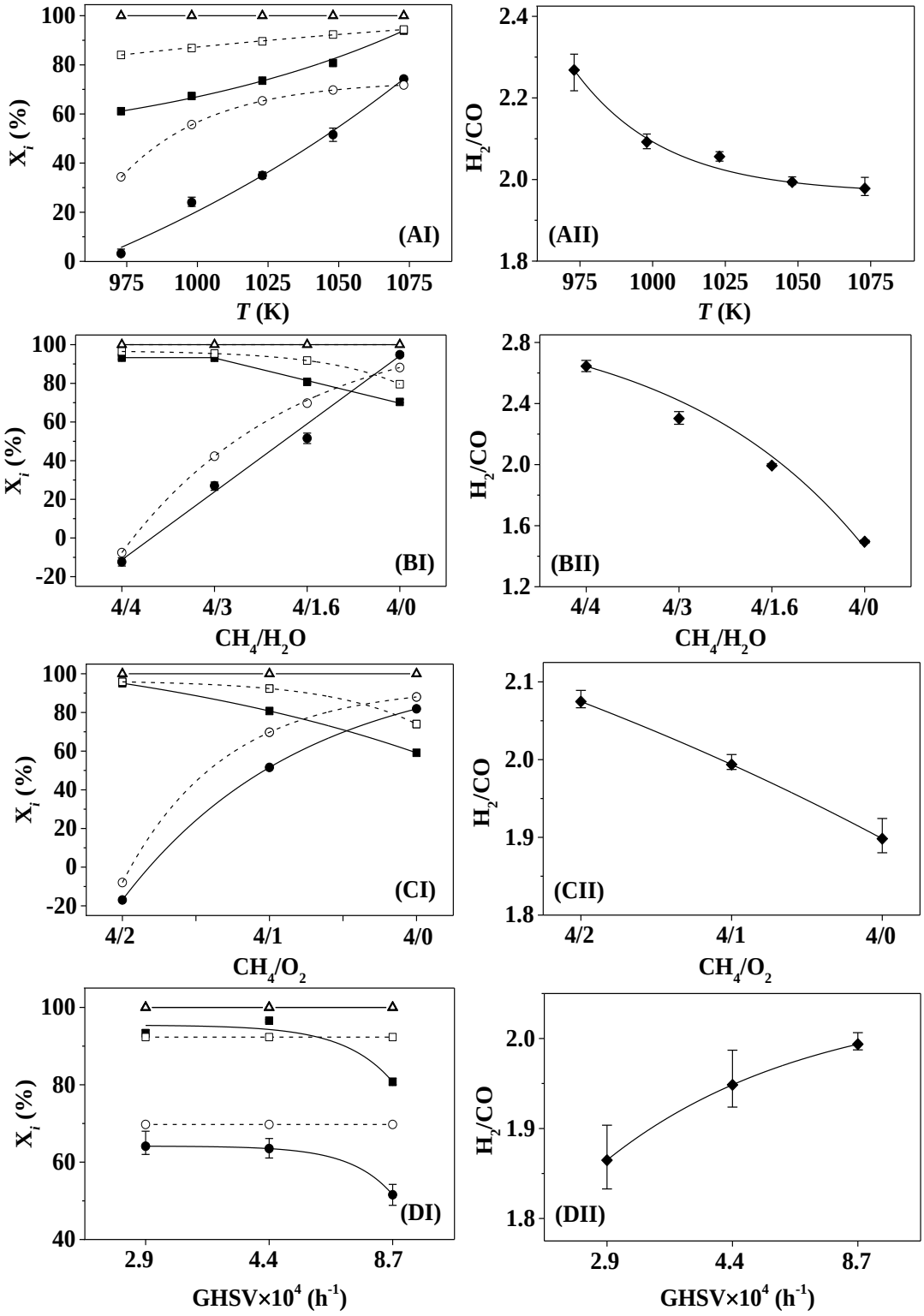

Fig. 9

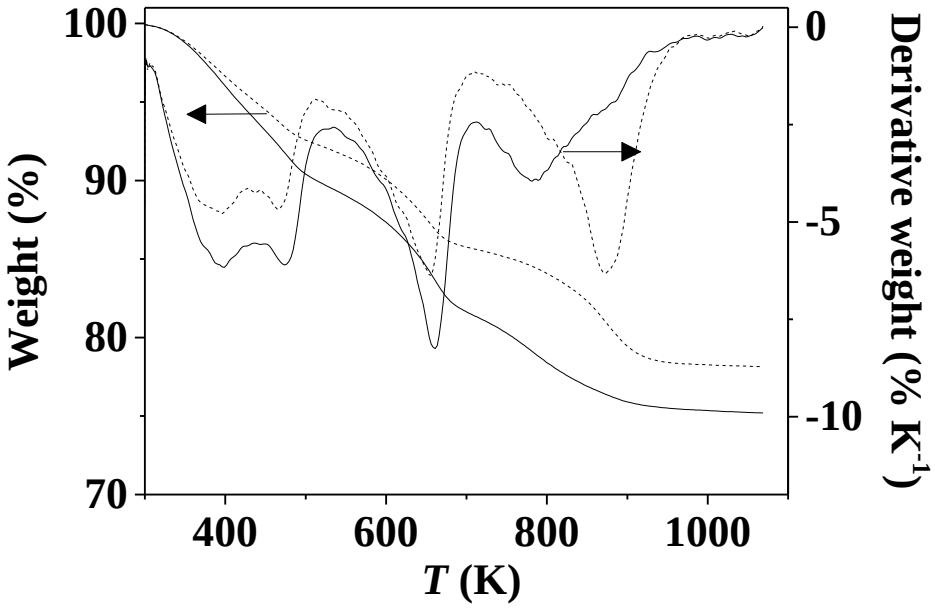

Fig. 10

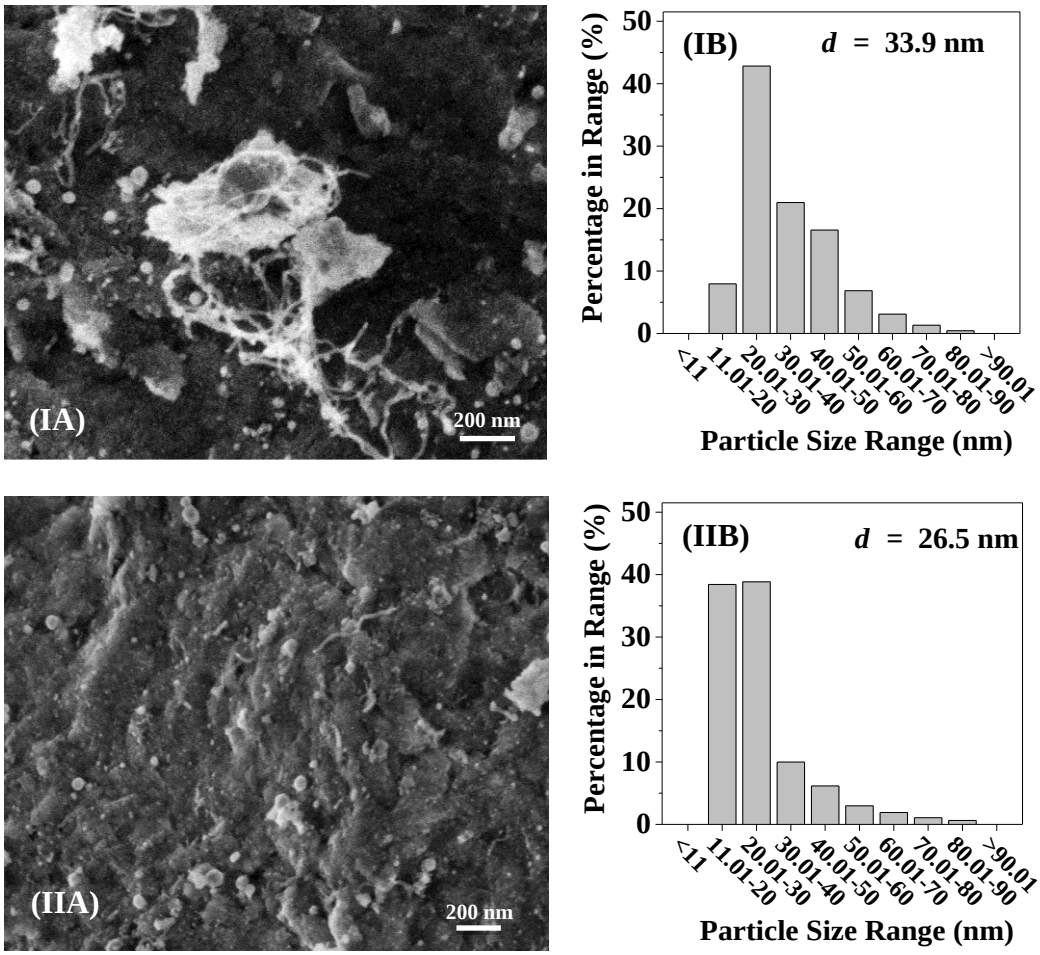

Fig. 11